PHYSICAL REVIEW B **101**, 014426 (2020)

Computational screening of Fe-Ta hard magnetic phases

S. Arapan,[1,*] P. Nieves,[1,2] H. C. Herper,[3] and D. Legut[1,4]
[1] IT4Innovations, VŠB—Technical University of Ostrava, 17. listopadu 2172/15, 70800 Ostrava-Poruba, Czech Republic
[2] ICCRAM, International Research Center in Critical Raw Materials and Advanced Industrial Technologies, Universidad de Burgos, 09001 Burgos, Spain
[3] Department of Physics and Astronomy, Uppsala University, Box 516, 75121 Uppsala, Sweden
[4] Nanotechnology Centre, VŠB—Technical University of Ostrava, 17. listopadu 2172/15, 70800 Ostrava-Poruba, Czech Republic

(Received 24 October 2019; revised manuscript received 7 December 2019; published 21 January 2020)

In this paper, we perform a systematic calculation of the Fe-Ta phase diagram to discover hard magnetic phases. By using structure prediction methods based on evolutionary algorithms, we identify two energetically stable magnetic structures: a tetragonal Fe_3Ta (space group 122) and a cubic Fe_5Ta (space group 216) binary phase. The tetragonal structure is estimated to have both high saturation magnetization ($\mu_0 M_s = 1.14$ T) and magnetocrystalline anisotropy ($K_1 = 2.17$ MJ/m^3) suitable for permanent magnet applications. The high-throughput screening of magnetocrystalline anisotropy also reveals two low-energy metastable hard magnetic phases: Fe_5Ta_2 (space group 156) and Fe_6Ta (space group 194), that may exhibit intrinsic magnetic properties comparable to $SmCo_5$ and $Nd_2Fe_{14}B$, respectively.

DOI: 10.1103/PhysRevB.101.014426

I. INTRODUCTION

Many technological applications used for information storage and green-energy generation, like motors for hybrid and electric cars and direct-drive wind turbines, rely on high quality permanent magnets (PMs) [1]. The increasing importance of PMs in modern society has resulted in a renewed interest in the design of new magnet materials that are cheaper and contain less critical components like rare earth (RE). One possible alternative to RE-PM could be RE-free Fe(Co)-rich intermetallic compounds. To be viewed as a good PM, a ferromagnetic compound must have a high Curie temperature ($T_C > 400$ K), a high saturation magnetization ($\mu_0 M_S > 1$T), and a high magnetocrystalline anisotropy energy (MAE), $K_1 > 1/\text{MJ/m}^3$, since large anisotropy is a key factor for the large coercivity needed for high-performance PMs [2]. In particular, from a technological point of view, it is important that the relation between MAE and saturation magnetization gives a magnetic hardness parameter $\kappa = \sqrt{K_1/(\mu_0 M_S^2)}$ greater than 1, thus, magnets can be used in any shape providing a good performance [3]. Although high values of saturation magnetization are desirable for creating strong magnetic fields, it decreases κ due to the induced demagnetizing field effects. The main contribution to the magnetic anisotropy is usually magnetocrystalline (K), that is, a combined effect of crystal-field splitting (or band formation) and spin-orbit coupling. This mechanism is also responsible for the surface, interface, and magnetostrictive anisotropies. Since none of the $4d$ and $5d$ dopants are ferromagnetic at room temperature, the $3d$ sublattice must spin-polarize the partially filled $4d/5d$ shells. This ensures a net spin-orbit effect, as required for the creation of the anisotropy. Therefore, the addition of heavy elements for a large spin-orbit coupling, such as Hf, Ta, Bi, Sn, or Zr, to the Fe-Co alloys could form hard magnetic phases suitable for PM applications with a low raw materials cost. However, a large magnetocrystalline anisotropy (MCA) in Fe-based alloys can only be found in noncubic uniaxial structures, like FePt where a large $K = 7$ MJ/m^3 is observed in the tetragonal $L1_0$ structure [4]. Therefore, the theoretical research of such compounds should be focused on noncubic uniaxial structures as tetragonal, hexagonal, or rhombohedral.

In Fe-Co alloys, Ta can induce some interesting features. For instance, recent gradient-composition sputtering experiments made by Phuoc *et al.* [5,6] showed that Co-Fe-Ta exhibits a peculiar increased magnetic anisotropy with temperature much larger than Fe-Co-M where $M =$ Hf, Zr, Lu. An improved coercivity has been reported in magnets such as $(Fe,Co)_2B$ and $Ce(Co,Fe,Cu)_5$ after the incorporation of a small amount of Ta [7,8]. While the Co-Ta phase diagram shows up to seven stable binary phases [9,10], only two structures have been found in the phase diagram of Fe-Ta: Laves phase (C14) Fe_2Ta space group (SG) 194, $P6_3/mmc$ and μ-phase FeTa SG 166, $R\text{-}3m$. The Fe_2Ta structure is a paramagnet in which either Fe or Ta excess can induce a ferromagnetic ordering at low temperatures ($\lesssim 150$ K) [11]. Theoretical calculations show an easy cone magnetocrystalline anisotropy in the ferromagnetic state [12]. Recently, Gabay and Hadjipanayis reported melt-spun alloys made of Fe-rich Fe_2Ta and Fe-bcc without sufficiently high coercivities (around 0.5 kOe at room temperature) for PM applications [13]. The other known stable crystalline phase, μ-phase FeTa, is an antiferromagnet with Néel temperature around 336 K [14]. Additionally, a small amount of Ta can also be inserted into the Fe-bcc structure [9]. In the case of structurally amorphous systems, Fe_9Ta thin films have been found to exhibit characteristics of a soft ferromagnetic material with

---

[*] Corresponding author: sergiu.arapan@gmail.com

very low coercivities (1−10 mT), saturation magnetization around 2 T, and extraordinary Hall effect [15].

In this paper, we performed a systematic computational exploration of Fe-rich Fe-Ta compounds to find magnetic structures with intrinsic properties suitable for high-performance PMs. The theoretical search for these magnetic phases is done in few stages. First, we searched for stable and low-energy metastable structures for different Fe-rich $Fe_{1-x}Ta_x$ binaries. Details of calculations and results of the crystal phase exploration are presented in the Sec. II. Second, a set of structures with intrinsic magnetic properties fulfilling the initial criteria of a good PM, i.e., exhibiting negative enthalpy of formation, $\Delta H < 0$, high saturation magnetization, and a uniaxial lattice, are selected from the collection of predicted structures as well as from the AFLOW database [16]. We calculate the MCA of all these phases and identify a smaller subset of structures, which exhibit intrinsic properties of hard magnets. These few phases are analyzed in more detail to understand the possible mechanisms of a high MCA in RE-free intermetallic compounds. We present the corresponding results and calculation details in Sec. III and Appendix A. At the third stage, we include the effects of finite temperature on the phase stability and performed calculations of the exchange integrals of the few selected structures to estimate the Curie temperature (T_C), thus, having screened all considered $Fe_{1-x}Ta_x$ binaries according to all three criteria to select a structure as a promising PM. Calculation details and results of this stage are presented in Sec. IV. We finalized our work by performing a study of a possible stabilization of metastable phases as thin films by epitaxial growth on suitable substrates. We performed calculations of the elastic properties of selected structures and results are given in Sec. V. The paper is completed by a Conclusions section.

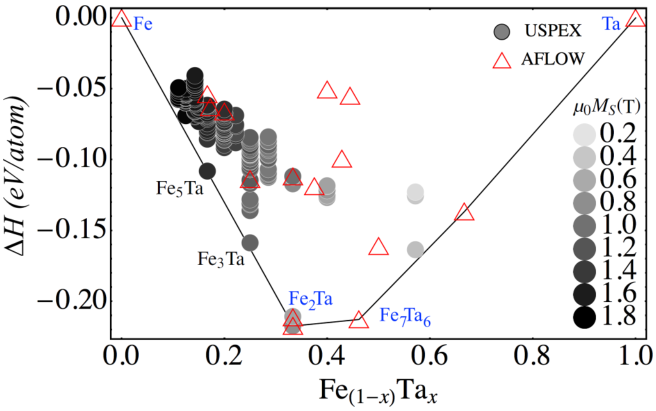

FIG. 1. Convex hull diagram of Fe-Ta showing phases predicted by using the USPEX (disks) and the reference structures from the AFLOW database (hollow red triangles). The magnitude of saturation magnetization is represented by the intensity of the gray scale. Experimentally observed phases for the Fe-Ta system are labeled in blue.

II. CRYSTAL PHASE SPACE EXPLORATION

We began our study by exploring the phase space of ordered Fe-rich $Fe_{1-x}Ta_x$ binaries for several compositions (Fe_2Ta, Fe_3Ta, Fe_4Ta, Fe_5Ta, Fe_5Ta_2, Fe_6Ta, Fe_7Ta, Fe_7Ta_2, $Fe_{17}Ta_3$, Fe_8Ta) using crystal predicting methods. Here, we follow an approach similar to the state-of-the-art Material Genome Initiative databases (AFLOW [16,17], Materials Project [18,19], etc.), where typically only ideal stoichiometric systems are considered. Nonstoichiometry effects can alter the phase stability and properties [20], but this analysis is beyond the scope of this paper. We searched for possible structures by using USPEX software [21,22], an implementation of the evolutionary algorithm, and the VIENNA AB INITIO SIMULATION PACKAGE (VASP) [23–25]. As in our recent work [26], we used an optimized USPEX-VASP interface for the efficient computational search of magnetic structures. We have run USPEX with the evolutionary algorithm method for 3D structures and choosing the enthalpy as a fitness criterion. The population size was set to be twice the number of atoms in the system and the maximum number of generations to be calculated was set to 40. We used 15 generations for convergence and the best 65% of the population size was used for new generation. Out of the new structures, 45% of were obtained by heredity, 5% by soft mutations, 5% by lattice mutations, and 45% were randomly generated. For the random generation, we used all space groups except triclinic and monoclinic lattice systems. All of the VASP calculations were done with the projector augmented wave (PAW) method [27] and the generalized gradient approximation (GGA) of Perdew, Burke, and Ernzerhof (PBE) [28] to the exchange correlation part of the energy functional (PAW PBE potentials version 5.4). We performed calculations with the p semicore electrons treated as valence ones. The best generated structures were fully relaxed until the maximum force component became less than 5×10^{-3} eV/Å. We used an automatic k-points generating scheme with the length $l = 40$ and an energy cutoff up to 1.4 of the default VASP energy cutoff. Additionally, we also ran calculations for a set of low-energy Fe-Ta phases close to convex hull available in the AFLOW database [16,17], which we use for reference. We present relevant results of this study in Fig. 1. This figure shows the convex hull diagram of the Fe-Ta binary system. The hull, shown by solid black lines, is formed by using calculated energies of the bcc Fe, bcc Ta, Fe_7Ta_6 (experimentally observed μ phase), and Fe_2Ta (theoretically predicted cubic phase SG 227 with the lowest calculated energy) phases. Symbols correspond to the values of enthalpy of formation ΔH of various phases with respect to single elements Fe and Ta as

$$\Delta H(\mathrm{Fe}_n\mathrm{Ta}_m) = E(\mathrm{Fe}_n\mathrm{Ta}_m) - n \cdot E(\mathrm{Fe}) - m \cdot E(\mathrm{Ta}), \quad (1)$$

where $E(.)$ is the energy at equilibrium conditions ($PV = 0$), n and m are the number of atoms of Fe and Ta in the formula unit of the Fe_nTa_m compound, respectively. $E(\mathrm{Fe})$ and $E(\mathrm{Ta})$ correspond to the energy of computationally optimized bcc phases of Fe and Ta. The relative position of these symbols with respect to the hull provides the information of the energy stability of structures at $T = 0$ K. Our search reveals a set of metastable magnetic phases (shown by filled disks) with two structures, a tetragonal Fe_3Ta (SG 122) and a cubic Fe_5Ta (SG 216), in the proximity of the convex hull. In addition, we show in Fig. 1 the magnitude of saturation magnetization of calculated phases, represented by the intensity of the gray scale. We can observe that all ferromagnetic Fe-Ta

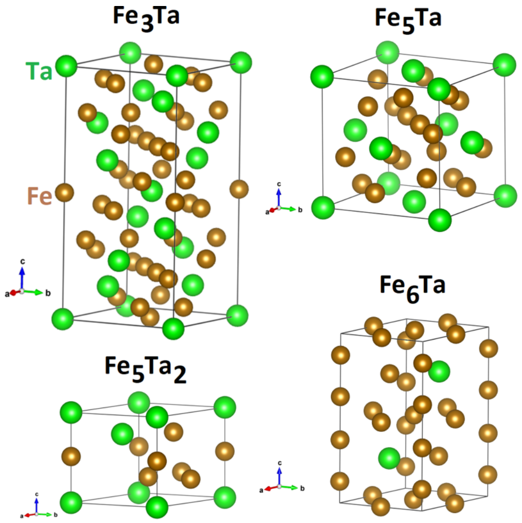

FIG. 2. Unit cells of four interesting theoretical Fe-Ta structures studied in this paper: Fe_3Ta (SG 122), Fe_5Ta (SG 216), Fe_6Ta (SG 194), and Fe_5Ta_2 (SG 156).

compounds with Fe content above 75 at. % have $\mu_0 M_S \gtrsim 1$ T. In this respect, the tetragonal Fe_3Ta also exhibits a saturation magnetization, which qualifies it as a promising PM structure. While the energetically stable Fe_5Ta phase is not suitable as a PM structure because of its cubic symmetry, it is interesting to analyze this phase in view of possible experimental synthesis as a validation of our theoretical predictions. More details of the Fe-Ta phases calculated with USPEX can be found in the Novamag database [29,30].

It is also worth pointing out that there are two other theoretical phases [16] on the Fe-Ta enthalpy hull that have not been observed in experiment. These phases are a cubic Fe_2Ta structure (SG 227 with six atoms in the primitive cell) and a tetragonal $FeTa_2$ structure (SG 140 with six atoms in the primitive cell). Quite interestingly, these structures are stable in the Co-Ta system. This discrepancy between calculations and experimental observations does not necessarily imply that the calculations are wrong, since the theoretical predictions are made for $T = 0$ K, while the experimentally observed phases are obtained from a Fe-Ta melt at quite high temperatures (of the order of 2000 K). One may not exclude the possibility that some of the theoretically predicted phases could be obtained by some low temperature synthesis. One of the main goals of our paper is to encourage trying different experimental techniques to obtain these phases.

III. SCREENING AND ANALYSIS OF MAGNETOCRYSTALLINE ANISOTROPY

A. High-throughput calculation of magnetocrystalline anisotropy

At the next stage of our study, we have performed calculations of MAE on a set of selected $Fe_{1-x}Ta_x$ binary structures. We screened a set of structures consisting of phases predicted by the USPEX search and phases available in the AFLOW database to select a subset of structures with $\Delta H < 0$, $\mu_0 M_S \gtrsim 1$ T, and a uniaxial lattice system (tetragonal, rhombohedral, and hexagonal). We calculated the MAE by performing VASP noncolinear spin-polarized calculations in a high-throughput manner [30]. Calculations of MAE require, usually, a higher accuracy, and, especially, a denser k mesh to sample the reciprocal space. This, inevitably, increases the amount of computational time and memory. To decrease the computational demand, we used the PAW PBE potential with a minimum number of valence electrons. Extended test calculations showed that the addition of the p semicore electrons do not change considerably calculated values (some detailed examples of the MAE calculations are provided in Appendix A). For all of the MAE calculations, we used an energy cutoff 1.50 times larger than the default one (ENCUT = 401.823 eV) and the energy of a system was calculated with a tolerance EDIFF = 10^{-9} eV. We also found that an automatic k-point mesh with the length $l = 60$ is enough to provide reliable MAE. The MAE was calculated as the energy difference between the configurations with different collinear spin arrangements divided by the unit cell volume,

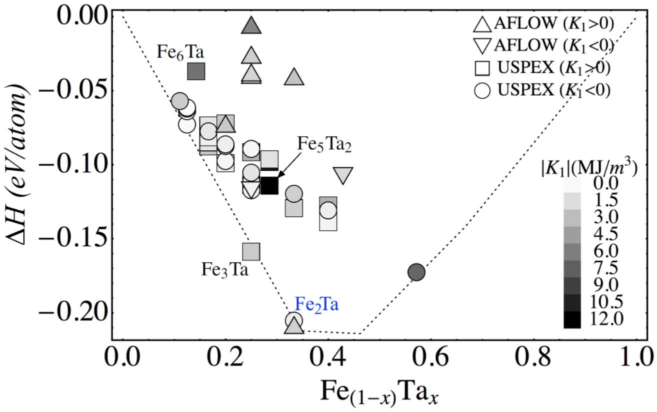

FIG. 3. Convex hull diagram of set of uniaxial Fe-Ta phases selected from the USPEX predicted phases and the AFLOW database. Gray scale represents the magnitude of the first MCA constant K_1. Various symbols correspond to the sign of K_1.

$$\Delta E(\theta) = E_\theta - E_{\theta=0}, \tag{2}$$

where θ is the angle between the direction of spins and the z axis. The energy of a given θ configuration, E_θ, was calculated in a non-self-consistent way by using the charge density and wave functions of a colinear spin-polarized calculation. We estimated the anisotropy constants K_1 and K_2 for uniaxial systems by fitting the MAE to the following equation:

$$\Delta E(\theta) = K_1 \sin^2(\theta) + K_2 \sin^4(\theta). \tag{3}$$

In Fig. 3, we show the convex hull diagram of uniaxial Fe-Ta phases obtained by performing the MAE calculations, where the magnitude of the first MCA constant K_1 is represented by the intensity of the gray scale and its sign by a given symbol. This figure reveals two hard magnetic phases: Fe_5Ta_2 (SG 156) with $\mu_0 M_S = 1$ T, $K_1 = 10.43$ MJ/m^3, and magnetic hardness parameter $\kappa = 3.62$, and Fe_6Ta (SG 194) with $\mu_0 M_S = 1.62$ T, $K_1 = 5.77$ MJ/m^3, and $\kappa = 1.66$. In the case of Fe_5Ta_2, the second MAE constant is also large and positive ($K_2 = 6.22$ MJ/m^3), so this phase exhibits a very high MAE barrier, $K_1 + K_2 = 16.65$ MJ/m^3. We can see that these values are comparable to the state-of-the-art RE-PM

TABLE I. Space group, enthalpy of formation, enthalpy of formation distance to the convex hull (ΔH_{hull}) according to Fig. 1, saturation magnetization, MCA constants, lattice parameters, temperature, Curie temperature, and magnetic hardness parameter of main Fe-Ta phases discussed in this paper. Data of $SmCo_5$ and $Nd_2Fe_{14}B$ are also shown for comparison. The chemical formula of known stable structures are written in bold.

Compound	Space group	ΔH (eV/atom)	ΔH_{hull} (meV/atom)	$\mu_0 M_s$ (T)	K_1 (MJ/m^3)	K_2 (MJ/m^3)	a (Å)	b (Å)	c (Å)	Temp (K)	T_C (K)	κ
Fe_2Ta	194	−0.2107	6.70	0.63	−0.73	1.48	4.776	4.776	7.824	0	–	–
Fe_2Ta [12]	194	−0.2350	–	0.66	−0.27	1.52	4.811	4.811	7.874	0	–	–
Fe_3Ta	122	−0.1588	4.28	1.14	2.17	−0.84	6.733	6.733	13.455	0	364	1.45
Fe_5Ta	216	−0.1083	0.43	1.53	–	–	6.678	6.678	6.678	0	–	–
Fe_5Ta_2	156	−0.1102	76.15	1.00	10.43	6.22	4.713	4.713	4.744	0	724	3.62
Fe_6Ta	194	−0.0662	26.94	1.62	5.77	0.60	4.627	4.627	9.353	0	886	1.66
$SmCo_5$ [31]	191	–	–	1.08	17.20	–	4.990	4.990	3.980	300	1020	4.30
$Nd_2Fe_{14}B$ [31]	136	–	–	1.61	4.90	–	8.790	8.790	12.180	300	588	1.54

$SmCo_5$ ($\mu_0 M_S = 1.08$ T, $K_1 = 17.2$ MJ/m^3) and $Nd_2Fe_{14}B$ ($\mu_0 M_S = 1.08$ T, $K_1 = 4.9$ MJ/m^3) at room temperature, respectively [31]. Here, we also highlight Fe_3Ta (SG 122) which combines both high phase stability (lays on the enthalpy convex hull) and good magnetic properties ($\mu_0 M_S = 1.14$ T and $K_1 = 2.17$ MJ/m^3). In Fig. 2, we show the unit cells of the above-mentioned structures: two new energetically stable phases Fe_3Ta (SG 122) and Fe_5Ta (SG 216), and two low-energy metastable hard magnetic phases Fe_5Ta_2 (SG 156) and Fe_6Ta (SG 194). In Tables I, II, and Appendix B we also provide various structural and magnetic properties of these phases. In the following sections, we analyze these four structures in more detail. To some extent, these results may also be applied to Fe-Nb or Fe-(Ta,Nb) systems due to the similarity between Ta and Nb. For instance, Fe_5Nb_2 (SG 156) also shows a large easy axis MAE with $K_1 = 7.7$ MJ/m^3 and $K_2 = 2.2$ MJ/m^3.

B. Analysis of the magnetocrystalline anisotropy for Fe_5Ta_2

To identify the source of the large MAE found above in Fe_5Ta_2 we follow a similar analysis as in Refs. [32,33]. Namely, we analyzed the spin-orbit coupling energy of each atom with all spin orientation along z and x axis, $E_{\mathrm{so}}[001]$ and $E_{\mathrm{so}}[100]$, see Table II. We observe that main contribution to total MAE comes from Fe and Ta atoms at the Wyckoff ($1a$) site with $\Delta E_{\mathrm{so}} = E_{so}[100] - E_{so}[001] = 3.04$ meV and 3.55 meV, respectively. Next, we try to find the main electronic states responsible for the large MAE. To do so, we analyzed the partial density of states (DOS) projected on the d states of Fe ($1a$) without including the spin-orbit coupling (SOC) interaction, see Fig. 4(a). It shows that there is a large DOS in the minority spin channel of the d_{xy} and $d_{x^2-y^2}$ states (d orbitals that lay on the hard plane) right at the Fermi level. This peak is decomposed into two smaller peaks below and above the Fermi level when the SOC is included and the magnetization is aligned along the easy axis [001], Fig. 4(b), decreasing the total energy and inducing a large MAE. The fact that the coupling between the minority spin channel gives the largest contribution to the SOC is also supported by the maximum values of the orbital magnetic moments in the easy direction of magnetization [12], as one can see in Table II. In the process of changing the direction of magnetization from the hard plane to easy axis, the SOC matrix element $\langle d_{xy}|\hat{H}_{\mathrm{so}}|d_{x^2-y^2}\rangle$ exhibits a much greater change than the other ones, Fig. 4(c). The total DOS with the SOC and spins along the hard plane (100) for the d_{xy} and $d_{x^2-y^2}$ orbitals [Fig. 4(b)] gives a very similar DOS as the partial DOS without the SOC included when adding the majority and minority spin channels for the d_{xy} and $d_{x^2-y^2}$ orbitals [derived from Fig. 4(a)]. In a few words, we could say that the reason for getting similar DOS within these two different calculations is because the d_{xy} and $d_{x^2-y^2}$ orbitals correspond to electronic states with the highest value of the z component of angular momentum (perpendicular to the x-y plane), so, if the spins are constrained to the x-y plane, then the SOC energy (proportional to the dot product between angular momentum and spin $\propto \hat{\mathbf{L}} \cdot \hat{\mathbf{S}}$) is very small. Hence, in this particular case, including the SOC for these orbitals with spins along the hard plane leads to a similar DOS as not including the SOC.

It is interesting to analyze in more detail the relation between the total energy and the SOC energy [32]. Let's write the total relativistic energy as $E = E_0 + E_{\mathrm{so}}$, where E_0 corresponds to the sum of kinetic and potential energies.

TABLE II. Crystallographic data, spin magnetic moment (μ_{spin}), orbital magnetic moment (μ_{orb}), and SOC energy (E_{so}) of Fe_5Ta_2 (SG 156).

Compound	Atom	Wyckoff position	x	y	z	$\mu_{\mathrm{spin}}[001]$ (μ_B)	$\mu_{\mathrm{orb}}[001]$ (μ_B)	$\mu_{\mathrm{spin}}[100]$ (μ_B)	$\mu_{\mathrm{orb}}[100]$ (μ_B)	$E_{\mathrm{so}}[100]$ (meV)	$E_{\mathrm{so}}[001]$ (meV)	ΔE_{so} (meV)
Fe_5Ta_2	Fe_1	$1a$	0	0	0.514	1.456	0.189	1.442	0.077	−17.403	−20.441	3.038
	Fe_2	$1b$	1/3	2/3	0.746	2.353	0.206	2.358	0.095	−17.395	−19.373	1.978
	Fe_3	$3d$	0.498	0.502	0.258	1.707	0.111	1.702	0.067	−16.559	−17.926	1.367
	Ta_1	$1c$	2/3	1/3	0.741	−0.536	0.072	−0.537	0.028	−288.187	−289.123	0.936
	Ta_2	$1a$	0	0	0	−0.524	0.052	−0.516	0.027	−297.208	−300.756	3.548

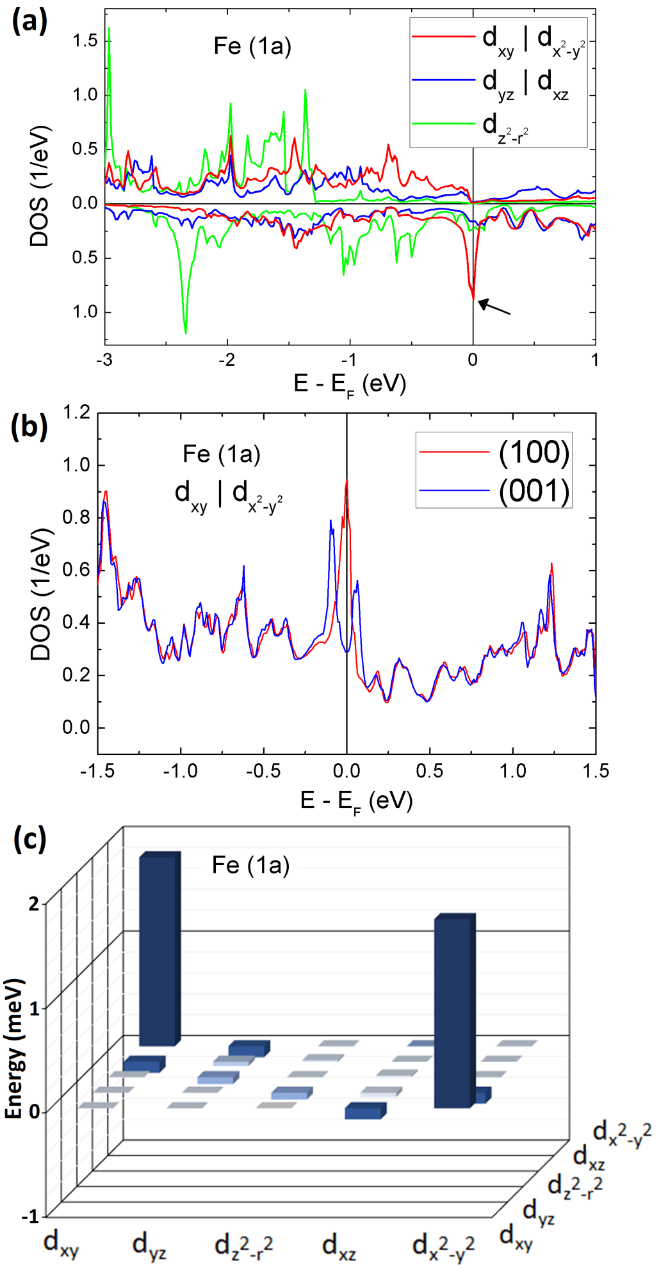

FIG. 4. (a) Partial DOS projected on d states of Fe atom at Wyckoff position ($1a$) of Fe$_5$Ta$_2$ without SOC interaction. (b) Total DOS projected on d$_{xy}$ and d$_{x^2-y^2}$ states of Fe ($1a$) in Fe$_5$Ta$_2$ when the magnetization is aligned along the easy axis (blue line) and hard plane (red line) including SOC interaction. (c) Change of the SOC matrix elements of Fe ($1a$) in Fe$_5$Ta$_2$, when magnetization goes from hard plane [100] to easy axis [001].

The ratio between the contribution to the MAE by the SOC ($\Delta E_{\mathrm{so}} = E_{\mathrm{so}}[100] - E_{\mathrm{so}}[001]$) and the total effective MAE ($\Delta E = E[100] - E[001]$) is typically close to 2 when the second-order perturbation theory holds, that is $\Delta E_{\mathrm{so}}/\Delta E \approx 2$. Hence, typically the total MAE is only around 50% of the SOC MAE [32] due to the SOC effects on the kinetic and potential energies $\Delta E_0 \approx -\Delta E_{\mathrm{so}}/2$, where $\Delta E_0 = E_0[100] - E_0[001]$. In the case of Fe$_5Ta_2$, we found that this MAE ratio is equal to $\Delta E_{\mathrm{so}}/\Delta E = 1.41$, thus, the total MAE is 71% of the SOC MAE thanks to a lower reduction induced by the SOC on the kinetic and potential energies ($\Delta E_0 = -0.29 \cdot \Delta E_{\mathrm{so}}$). This fact contributes to significantly enhancing the total MAE in the Fe$_5$Ta$_2$ phase. For instance, this MAE ratio is smaller than in the L1$_0$ FePt (1.84) and CoPt (1.67) [32].

IV. FINITE-TEMPERATURE EFFECTS: PHASE STABILITY AND THE CURIE TEMPERATURE

A. Phase stability at finite temperatures

For the four selected phases in the Fe$_3$Ta, Fe$_5$Ta, Fe$_5$Ta$_2$, and Fe$_6$Ta binaries, we further studied the effect of temperature and pressure on their structural stability. We have calculated the free energy by considering the lattice contribution in the quasiharmonic approximation and the entropy of electron system,

$$F(T) = E_0 + F_{\mathrm{ph}}(T) + F_{\mathrm{el}}(T), \tag{4}$$

where E_0 is the density-functional theory (DFT) energy at $T = 0K$, F_{ph} is the phonon free energy, and F_{el} is the free energy of electrons, estimated by the Sommerfeld formula [34],

$$F_{\mathrm{el}}(T) = -\frac{N(E_F)}{6}\pi^2 k_B^2 T^2, \tag{5}$$

where $N(E_F)$ is the DOS at the Fermi level.

Calculations were performed in the following manner. For each structure, we performed DFT calculations over a set of volumes $\{V_i\}$ $(i = 1, \ldots, 11)$ within an interval $(V_0 - \Delta V, V_0 + \Delta V)$ about equilibrium volume V_0, with $\Delta V = 0.1V_0$. Structures were relaxed at each volume and accurate total energy E_0 and DOS calculated. To calculate the phonon free energy F_{ph}, we used the PHON code [35], an implementation of the small displacements method to calculate phonon dispersion of a harmonic crystal. At each volume, supercells were generated from relaxed structures and forces were calculated with the VASP program. For these calculations, we used the PAW potentials containing the semicore p electrons, and performed accurate calculations with a cutoff energy of ENCUT = 513.167 eV (1.75 of the default cutoff energy) and the tolerance of the electronic convergence set to EDIFF = 10^{-7} eV. We used a fully automatic k-points generation mesh with length $l = 40$ to sample the reciprocal space. We have performed free energy calculations for the four above-mentioned structures, as well as for the two experimentally observed phases within the Fe-rich region: bcc Fe and Fe$_2$Ta. All phases were dynamically stable within the whole considered pressure range (no imaginary frequencies). To calculate the phase stability at finite temperatures and different pressures, we have estimated parameters of the equation of state (EOS) $F = F(V,T)$ at a set of temperature values within the (0 K, 1000 K) interval by fitting at each temperature T the set $\{F(V_i)\}$ of calculated free-energy values to the Vinet EOS [36]:

$$\begin{aligned} F(V) = F_0 &+ 4\frac{B_0V_0}{(B'-1)^2} - 2\frac{B_0V_0}{(B'-1)^2} \\ &\times [5 + 3B'(\eta(V) - 1) - 3\eta(V)] \\ &\times \exp\left[-\frac{3}{2}(B'-1)(\eta(V)-1)\right], \end{aligned} \tag{6}$$

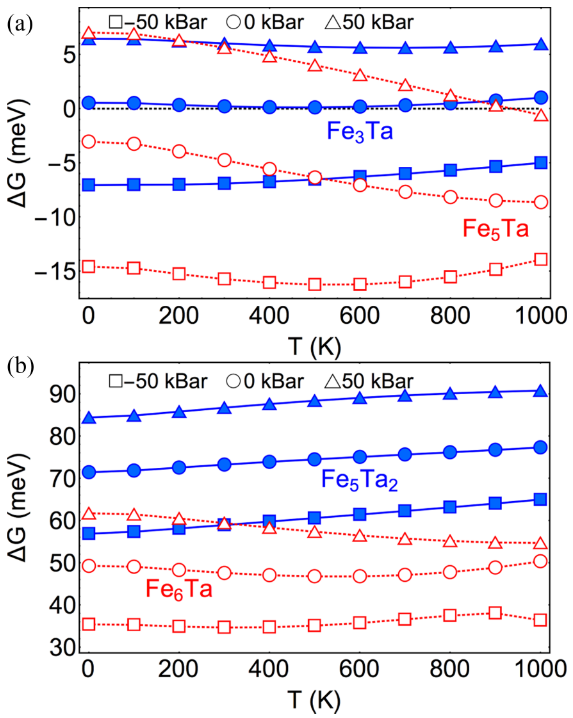

FIG. 5. Gibbs free-energy difference $\Delta G(T, P)$ of selected structures: (a) Fe_3Ta (blue filled symbols) and Fe_5Ta (red open symbols); (b) Fe_5Ta_2 (blue filled symbols) and Fe_6Ta (red open symbols); relative to stable bcc Fe and Fe_2Ta phases according to Eq. (7).

where $\eta(V) = (V/V_0)^{1/3}$ and $F_0 = F_0(T)$, $V_0 = V_0(T)$, $B_0 = B_0(T)$, and $B' = B'(T)$ are the equilibrium free energy, volume, bulk modulus, and its derivative at a given T. Within the Vinet approximation to the Helmholtz free energy, we calculated the Gibbs free energy $G(P, T) = F(V, T) + PV$ and estimated the formation energy with respect to stable bcc Fe and Fe_2Ta as

$$\Delta G = G(\mathrm{Fe}_n\mathrm{Ta}_m) - X_n G(\mathrm{Fe}) - Y_{nm} G(\mathrm{Fe_2Ta}), \qquad (7)$$

where X_n and Y_{nm} are appropriately chosen for each considered Fe_nTa_m phase. The temperature dependence of the formation energy of Fe_3Ta and Fe_5Ta, which were close to the enthalpy hull at $T = 0$ (Fig. 1) is shown in Fig. 5(a) for different pressures. Calculations show that the predicted cubic Fe_5Ta phase should be stable at ambient pressure (data shown by open disks) over the whole considered temperature range. The promising magnetic phase Fe_3Ta (shown by filled symbols) also remains very close to the stability line for the ambient pressure. At finite positive pressures (compression), both phases get energetically less stable. The effect is opposite for the negative pressure values (dilatation). This pressure effect suggests that the new phase may get energetically more stable by adding a third element, which would slightly increase the interatomic distances. In Fig. 5(b), we show the temperature and pressure trends for the formation energies of metastable Fe_5Ta_2 (filled symbols) and Fe_6Ta (open symbols) phases with high magnetic anisotropy. Both phases remain unstable with temperature and formation energies showing similar trends with pressure as in the case of Fe_3Ta and Fe_5Ta phases.

B. Exchange integrals and Curie temperature

Using the optimized geometries of the new phases as the starting point, the exchange coupling constants were calculated. The effective exchange interaction parameters were obtained using Lichtenstein *et al.'s* method [37,38], as implemented in SPR-KKR [39]. In this technique, the energy of the system is mapped onto a classical Heisenberg model with the following Hamiltonian:

$$E_{\mathrm{ex}} = -\sum_{i,j} J_{ij}\mathbf{s}_i \cdot \mathbf{s}_j, \qquad (8)$$

where J_{ij} are the exchange parameters and $\mathbf{s}_i$ is the unit vector along the magnetic moment of atom ith. The fast SPR-KKR core within atomic sphere approximation was used to obtain the exchange coupling constants. After a self-consistent run needed to create the potential for the systems, the J_{ij} were calculated using a dense k-point mesh 34 × 34 × 29 for Fe_5Ta_2 (SG 156). The cutoff for the J_{ij} couplings was chosen to be three lattice constants. The J_{ij} values obtained from the SPR-KKR code depending on the neighbor distance are shown in Fig. 6.

Due to the complexity of the structure, the Fe-Fe couplings of the Fe_5Ta_2 phase are very diverse. The contribution from Fe_1-Fe_1 ($1a$ site, along c axis) is quite small, being 5 meV for the nearest neighbors. The main contributions stem from Fe_2 and Fe_3 couplings. For these ions, the next-nearest-neighbor couplings are between 20 and 30 meV. However, the coupling strength rapidly decreases with the distance and is almost zero after five neighbor shells. It should be pointed out that the majority of the coupling constants are positive, which means ferromagnetic coupling. Only very tiny small antiferromagnetic contributions were observed for Fe_5Ta_2 (Fe_3). However, even though Ta has only an induced moment, there are significant couplings between Ta and the Fe ions, especially Fe_1. Unfortunately, the coupling is antiferromagnetic and therewith counteracts to a high T_C.

Finally, we estimated the T_C of these phases by means of atomistic spin dynamics simulations [40], using as inputs the calculated lattice parameters, exchange parameters, and magnetic moments. For each structure, we consider a system of 15 × 15 × 15 unit cells with periodic boundary conditions, which is thermally relaxed, integrating the stochastic Landau-Lifshitz-Gilbert equation. We performed this task with the software UPPASD [41,42]. The obtained values for Fe_3Ta, Fe_5Ta_2, and Fe_6Ta are $T_C = 364$ K, 724 K, and 886 K, respectively, that make them suitable for PM applications. However, the performance of Fe_3Ta may be highly deteriorated at room temperature since T_C is not so large. It should be noted that despite the fact that there are stronger antiferromagnetic Fe-Ta coupling parameters for Fe_5Ta_2 and Fe_6Ta than for Fe_3Ta, the Curie temperatures for these systems are higher than for Fe_3Ta. This is partially related to the multiplicity of

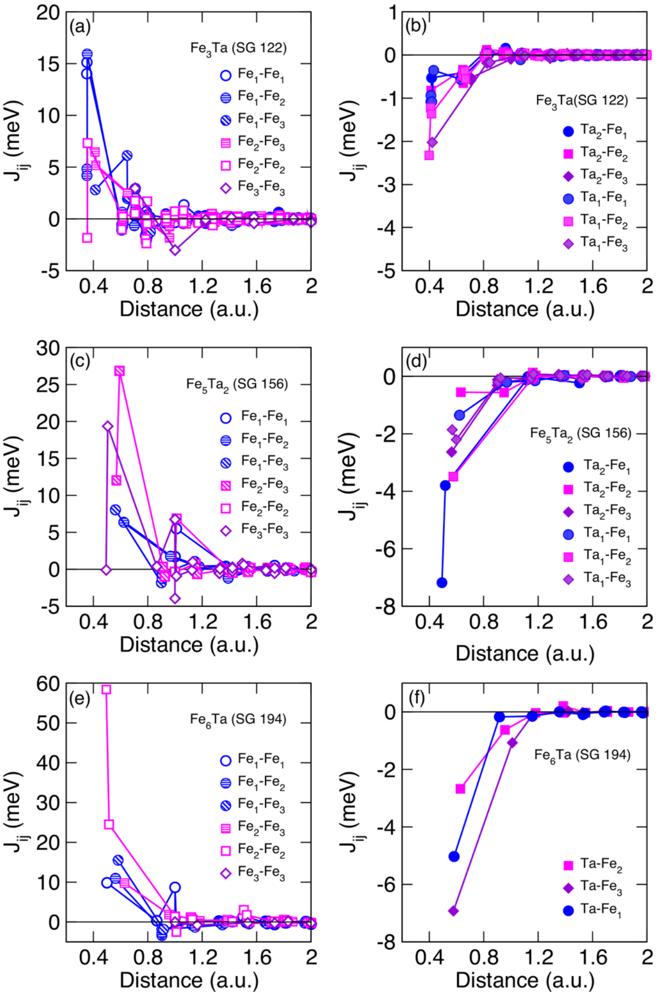

FIG. 6. Calculated exchange coupling constants for: (a), (b) Fe_3Ta; (c), (d) Fe_5Ta_2; and (e), (f) Fe_6Ta, depending on the distance between the ions. Left: The couplings between the Fe ions in the system are shown. Right: The couplings between the magnetic Fe ions and the Ta ions (which have an induced moment antiparallel to the Fe atoms) are plotted. Note the different scale between the two graphs.

the individual couplings but also to the fact that the Fe-Fe couplings in Fe_3Ta are smaller.

V. SCREENING OF SUBSTRATES FOR EPITAXIAL STABILIZATION

As we mentioned in the Introduction, only two stable phases have been experimentally identified for the Fe-Ta binaries so far. Our theoretical predictions seem to contradict this fact, but there may exist a possibility that observing these phases is difficult when synthesizing the Fe-Ta alloys with traditional metallurgical methods [43]. Of course, these methods are preferable to produce a bulk PM suitable for applications. Right now, however, we would be more interested in the possibility to synthesize predicted phases and probe their magnetic properties to assess the predictive accuracy of our computational methods. One may try to stabilize some of these phases as thin films by epitaxial growth. Thus, as a final stage of our work, we performed a screening of suitable substrates that may help to stabilize these phases. Here, we follow the methodology described in Ref. [44]. This approach uses two types of substrate filters based on the unit cell topology (geometric unit cell area matching between the substrate and the target film) and strain energy density of the film to identify ideal substrates for epitaxial stabilization [44].

We performed this task using the modules implemented in PYMATGEN library [45]. For substrate candidates, we have used the full Materials Project substrate database [18,19] that contains 78 widely used single-crystalline materials (heterostructural epitaxy approach) [44] via PYMATGEN.EXT.MATPROJ module. For the films, we selected Fe_5Ta_2 (SG 156), Fe_3Ta (SG 122), Fe_6Ta (SG 194), and Fe_5Ta (SG 216). In our calculations, as film input data, we used the crystallography information of the relaxed unit cells, so the film is considered as a perfect monocrystalline material, as well as their elastic constants. The film/substrate orientations were obtained by using existing surface and symmetry tools within PYMATGEN to generate all possible surface orientations [44–46]. The substrate-film boundary condition assumes that the substrate surface is rigid with no structural relaxation perpendicular to the epitaxy plane. Hence, the strain energy (ΔE_s) imposed on the film can be expressed as $\Delta E_s = V \cdot e^{\mathrm{plane}}$, where V is the volume of the film per atom and e^{plane} is the film strain energy density induced in the epitaxy plane. The film strain energy density is calculated as [44] $e^{\mathrm{plane}} = VC^{*}_{ijkl}\epsilon^{\mathrm{plane}}_{ij}\epsilon^{\mathrm{plane}}_{kl}/2$, where C^{*}_{ijkl} is obtained by the transformation of the fourth-order elastic tensor C_{ijkl} into the lattice orientation correspondence between the substrate and the film, and ϵ denotes the strain. The elastic constants needed for the calculation of the film elastic energy were obtained through AELAS code [47] combined with VASP using PAW method and GGA-PBE with default settings. In Table V (Appendix C), we show the calculated elastic constants of these selected film Fe-Ta phases, as well as bulk modulus, Young's modulus, shear modulus, and Poisson's ratio in Hill approximation. These elastic tensors fulfill all necessary and sufficient conditions for elastic stability [48]. The unit cell topology filter is based on the Zur and McGill algorithm [44,49] that systematically searches for all possible matches between various faces of the substrate and film, aiming to find low coincident area of matching 2D superlattices. Through this method, for each pair of substrate and film, one value of minimal common unit cell area can be obtained, called minimal coincident interfacial area (MCIA)[44].

In Fig. 7, we show the high-throughput calculation of the MCIA and elastic energy of Fe_5Ta_2 for all considered substrates and orientations. Optimal substrates are those with both low values of MCIA and elastic energy. In this case, the best substrates are (001)-MgF_2 (001)-TiO_2 and (001)-Al_2O_3 with Fe_5Ta_2 film orientation (100), (100), and (001), respectively. The obtained values of MCIA and elastic energy for the substrates with the lowest value of MCIA are given in Table IV (Appendix C). Although bulk Fe_5Ta is not a good PM (cubic phase), its phase stability is greater than the above-mentioned ones (see Fig. 5). Our calculations show that potential good substrates for Fe_5Ta could be (001)-MgF_2, (100)-InSb, and (100)-CdTe with film orientation (100).

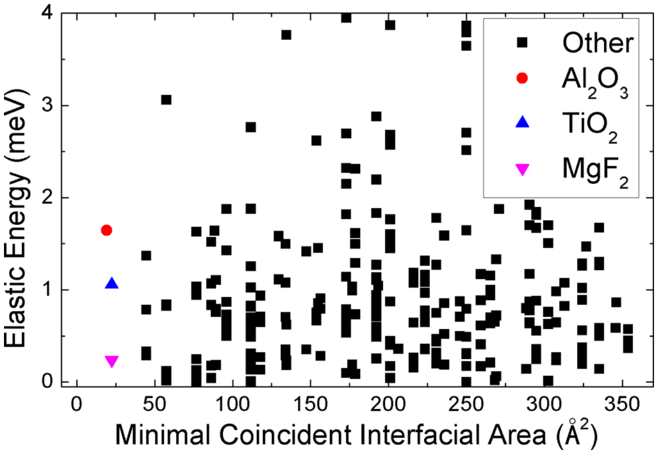

FIG. 7. Computational screening of substrates for the epitaxial stabilization of Fe_5Ta_2.

VI. CONCLUSIONS

Despite the fact that the two experimentally observed ordered Fe-Ta alloy phases do not exhibit magnetic properties suitable for PMs, our computational study suggests that new phases, with intrinsic magnetic properties appropriate for PMs, might exist within this binary system. The structure prediction study based on an evolutionary algorithm revealed two energetically stable structures for the Fe_5Ta and Fe_3Ta binaries, respectively. Fe_3Ta is a uniaxial phase (tetragonal symmetry) with calculated saturation magnetization $\mu_0 M_s =$ 1.14 T, magnetocrystalline anisotropy K_1=2.17 MJ/m^3, and the Curie temperature $T_C = 364$ K, which makes it a potentially promising phase for PMs. Calculations of MAE of various low-energy metastable phases also showed the existence of structures with extraordinary high MAE in the Fe-Ta system. We identified two phases in the Fe_5Ta_2 and Fe_6Ta binaries with intrinsic magnetic properties comparable to $SmCo_5$ and $Nd_2Fe_{14}B$, respectively. For the Fe_5Ta_2 structure, for example, our calculations predict $\mu_0 M_s = 1.00$ T, K_1+K_2=16.65 MJ/m^3, and $T_C = 724$ K. In this phase, we found that there is a large DOS in the minority spin channel of the d_{xy} and $d_{x^2-y^2}$ states (d orbitals that lay on the hard plane) right at the Fermi level for both Fe and Ta atoms at the Wyckoff (1a) site, which may be responsible for the high calculated MAE. It is necessary, of course, to analyze more hard intermetallic Fe-based phases to identify possible general mechanisms of high MAE. The analysis of the Gibbs free energy shows that these hard magnetic phases are

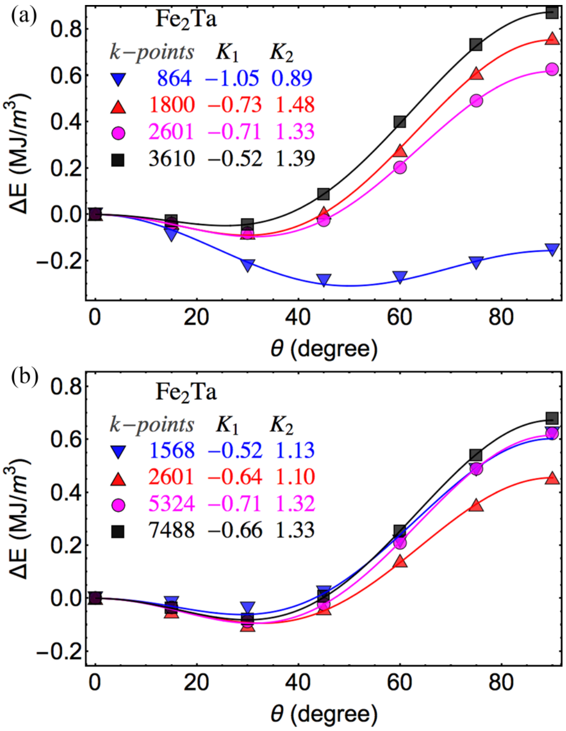

FIG. 8. Magnetocrystalline anisotropy energy of the ferromagnetic Laves Fe_2Ta phase calculated for different number of k points in the reciprocal space: (a) calculations performed with PAW PBE potentials with the minimum number of valence electrons and cutoff energy of 401.823 eV (1.50 of the default cutoff energy); (b) calculations performed with PAW PBE potentials with the p semicore electrons added to the valence electrons and cutoff energy of 513.167 eV (1.75 of the default cutoff energy).

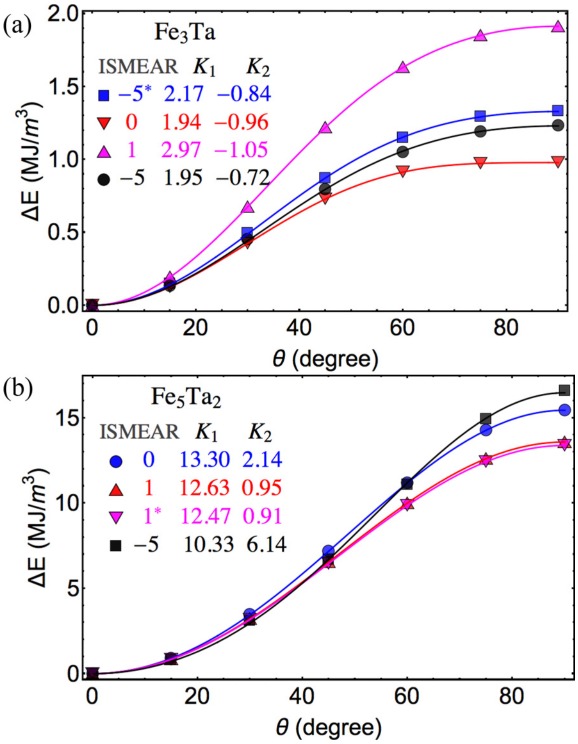

FIG. 9. Magnetocrystalline anisotropy energy of predicted (a) Fe_3Ta and (b) Fe_5Ta_2 phases calculated for different settings for the smearing parameter ISMEAR = 0, 1, −5 (Gaussian, first-order Methfessel-Paxton and tetrahedron with Blöchl corrections methods, respectively). For all the calculations, except those marked with an asterisk, we used the PAW PBE potentials with minimum number of valence electrons, a k mesh corresponding to length $l = 60$, and energy cutoff of 401.823 eV (1.50 of the default cutoff energy). For the other two calculations marked with an asterisk, we used the PAW PBE potentials with the p semicore electrons added to the valence electrons and cutoff energy of 513.167 eV (1.75 of the default cutoff energy).

energetically unstable at finite temperatures too, so this may prevent the synthesis of these phases in bulk. It might be possible, however, to synthesize these phases as thin films and we provide some possible substrates for the epitaxial growth. These findings might constitute a step forward toward the discovery and design of novel high-performance RE-free PMs.

ACKNOWLEDGMENTS

This work was supported by the European Horizon 2020 Framework Programme for Research and Innovation (2014-2020) under Grant Agreement No. 686056, NOVAMAG. Authors acknowledge the European Regional Development Fund in the IT4Innovations National Supercomputing Center, path to exascale project, Project No. CZ 02.1.01/0.0/0.0/16-013/0001791 within the Operational Programme Research, Development and Education. D.L. acknowledges the Czech Science Foundations Grant No. 17-23964S.

APPENDIX A: SOME DETAILS OF CALCULATIONS OF MAE

In this Appendix, we show some tests of our MAE calculations for Laves phase Fe_2Ta, and theoretically predicted Fe_3Ta (SG 122) and Fe_5Ta_2 (SG 156). The Fe_2Ta phase was theoretically investigated previously [12,50] with contradictory results for the MAE calculations using different DFT codes. In Fig. 8, we show calculated MAE with VASP code for different k-point meshes as well as different PAW PBE potentials and cutoff energies. We can see that calculated values of the MAE are quite robust against different PAW PBE potentials and are converged for a number of k points in the reciprocal space larger than 1500, which corresponds to the length $l = 60$ in the VASP automatic k-points generation scheme. These results are in agreement with those reported by Edström [12], who also obtained an easy cone for the MCA with $K_1 = -0.27$ MJ/m^3 and $K_2 = 1.52$ MJ/m^3. The value of the MAE of 1.25 MJ/m^3 is larger than the one we have obtained (Fig. 8) due to the larger cell volume used in Ref. [12], see Table I.

The Fe_3Ta and Fe_5Ta_2 phases present a particular interest. The first one is energetically very close to the convex hull of the Fe-Ta binary diagram and, thus, could be experimentally obtained under appropriate conditions. The relatively high saturation magnetization and magnetocrystalline anisotropy make this phase a promising candidate for RE-free PM material. The second one, despite being metastable, provides an example of huge MCA for a RE-free intermetallic compound. We have performed a series of MAE calculations for different parameters which affects the energy calculations, like the type of PAW PBE potentials, energy cutoff, and energy smearing. These additional calculations are shown in Fig. 9. We see that results of the MAE calculations are robust against the variations of these parameters.

APPENDIX B: CRYSTALLOGRAPHIC AND MAGNETIC DATA

In this Appendix, we provide the crystallographic data and magnetic moments of three selected Fe-Ta phases (see Table III).

TABLE III. Crystallographic data and spin magnetic moment of Fe_3Ta (SG 122), Fe_6Ta (SG 194), and Fe_5Ta (SG 216).

Compound	Atom	Wyckoff position	x	y	z	$\mu_{\text{spin}}[001]$ (μ_B)
Fe_3Ta	Fe_1	16e	0.876	0.374	0.436	1.727
	Fe_2	16e	0.626	0.874	0.061	1.646
	Fe_3	4b	0	0	1/2	2.564
	Ta_1	8d	0.731	1/4	0.125	−0.382
	Ta_2	4a	0	0	0	−0.354
Fe_6Ta	Fe_1	6g	1/2	0	0	1.921
	Fe_2	4e	0	0	0.628	2.436
	Fe_3	2d	1/3	2/3	3/4	2.305
	Ta_1	2c	1/3	2/3	1/4	−0.890
Fe_5Ta	Fe_1	16e	0.625	0.625	0.625	1.939
	Fe_2	4c	1/4	1/4	1/4	2.746
	Ta_1	4a	0	0	0	−0.438

APPENDIX C: OPTIMAL SUBSTRATES INFORMATION FOR EPITAXIAL GROWTH AND ELASTIC PROPERTIES

In this Appendix, we provide information about three optimal substrates for each of selected Fe-Ta films (Table IV). Additionally, we include the calculated elastic tensor and derived elastic properties of selected Fe-Ta phases (Table V). The details of these calculations are described in Sec. V.

TABLE IV. Optimal substrates for epitaxial growth of phases Fe_5Ta_2 (SG 156), Fe_3Ta (SG 122), Fe_6Ta (SG 194), and Fe_5Ta (SG 216).

Film	Film orientation	Substrate	Substrate orientation	MCIA (Å^2)	Elastic energy (meV)
Fe_5Ta_2	⟨001⟩	Al_2O_3	⟨001⟩	19.24	1.645
	⟨100⟩	TiO_2	⟨001⟩	22.36	1.058
	⟨100⟩	MgF_2	⟨001⟩	22.36	0.239
Fe_3Ta	⟨001⟩	MgF_2	⟨001⟩	45.34	0.795
	⟨001⟩	InSb	⟨100⟩	45.34	0.881
	⟨001⟩	CdTe	⟨100⟩	45.34	0.956
Fe_6Ta	⟨100⟩	MgF_2	⟨100⟩	43.29	0.213
	⟨100⟩	MgF_2	⟨001⟩	43.29	0.332
	⟨100⟩	TiO_2	⟨001⟩	43.29	0.041
Fe_5Ta	⟨100⟩	MgF_2	⟨001⟩	44.59	0.124
	⟨100⟩	InSb	⟨100⟩	44.59	0.158
	⟨100⟩	CdTe	⟨100⟩	44.59	0.189

TABLE V. Independent elastic tensor elements c_{ij}, bulk modulus B, Young's modulus E, shear modulus G, and Poisson's ratio ν in Hill approximation of Fe_5Ta_2 (SG 156), Fe_3Ta (SG 122), Fe_6Ta (SG 194), and Fe_5Ta (SG 216).

Film	Elastic tensor element	c_{ij} (GPa)	B (GPa)	E (GPa)	G (GPa)	ν
Fe_5Ta_2	c_{11}	343.45	219.71	231.57	87.43	0.324
	c_{12}	179.96				
	c_{13}	143.57				
	c_{33}	357.09				
	c_{44}	83.48				
	c_{14}	-5.64				
Fe_3Ta	c_{11}	345.07	225.97	269.01	103.34	0.302
	c_{12}	166.52				
	c_{13}	165.59				
	c_{33}	348.18				
	c_{44}	114.37				
	c_{66}	111.04				
Fe_6Ta	c_{11}	342.79	195.80	247.55	96.00	0.289
	c_{12}	148.58				
	c_{13}	111.34				
	c_{33}	336.73				
	c_{44}	84.92				
Fe_5Ta	c_{11}	296.93	210.29	203.92	76.18	0.338
	c_{12}	166.97				
	c_{44}	84.72				

[1] G. Scheunert, O. Heinonen, R. Hardeman, A. Lapicki, M. Gubbins, and R. M. Bowman, Appl. Phys. Rev. **3**, 011301 (2016).

[2] K. Skokov and O. Gutfleisch, Scr. Mater. **154**, 289 (2018).

[3] R. Skomski and J. M. D. Coey, Scr. Mater. **112**, 3 (2016).

[4] O. A. Ivanov, L. V. Solina, V. A. Demshina, and M. L. Magat, Fiz. Metal. Metalloved. **35**, 92 (1973).

[5] N. N. Phuoc and C. K. Ong, IEEE Trans. Magn. **50**, 1 (2014).

[6] N. N. Phuoc, P. Chapon, O. Acher, and C. K. Ong, J. Appl. Phys. **114**, 153903 (2013).

[7] S. Taskaev, K. Skokov, V. Khovaylo, D. Gunderov, and D. Karpenkov, Phys. Procedia **75**, 1404 (2015).

[8] T. N. Lamichhane, M. T. Onyszczak, O. Palasyuk, S. Sharikadze, T.-H. Kim, Q. Lin, M. J. Kramer, R. W. McCallum,

A. L. Wysocki, M. C. Nguyen, V. P. Antropov, T. Pandey, D. Parker, S. L. Budko, P. C. Canfield, and A. Palasyuk, Phys. Rev. Appl. **11**, 014052 (2019).

[9] P. Villars, K. Cenzual, and R. Gladyshevskii, *Handbook of Inorganic Substances 2014* (De Gruyter, Berlin and Boston, 2014).

[10] K. Shinagawa, H. Chinen, T. Omori, K. Oikawa, I. Ohnuma, K. Ishida, and R. Kainuma, Intermetallics **49**, 87 (2014).

[11] K. Kai, T. Nakamichi, and M. Yamamoto, J. Phys. Soc. Jpn. **29**, 1094 (1970).

[12] A. Edström, Phys. Rev. B **96**, 064422 (2017).

[13] A. M. Gabay and G. C. Hadjipanayis, AIP Adv. **9**, 035143 (2019).

[14] M. Ahmed, G. Hallam, and D. Read, J. Magn. Magn. Mater. **37**, 101 (1983).

[15] S. Shaji, N. R. Mucha, A. Majumdar, C. Binek, A. Kebede, and D. Kumar, J. Magn. Magn. Mater. **489**, 165446 (2019).

[16] AFLOWLIB, http://aflowlib.org.

[17] S. Curtarolo, W. Setyawan, S. Wang, J. Xue, K. Yang, R. H. Taylor, L. J. Nelson, G. L. Hart, S. Sanvito, M. Buongiorno-Nardelli *et al.*, Comput. Mater. Sci. **58**, 227 (2012).

[18] A. Jain, S. Ong, G. Hautier, W. Chen, W. Richards, S. Dacek, S. Cholia, D. Gunter, D. Skinner, G. Ceder *et al.*, APL Mater. **1**, 011002 (2013).

[19] The Materials Project, https://materialsproject.org

[20] J.-L. Zhang and G.-Y. Hong, in *Modern Inorganic Synthetic Chemistry*, 2nd ed., edited by R. Xu and Y. Xu (Elsevier, Amsterdam, 2017), pp. 329–354, http://www.sciencedirect.com/science/article/pii/B9780444635914000136

[21] A. O. Lyakhov, A. R. Oganov, H. T. Stokes, and Q. Zhu, Comput. Phys. Commun. **184**, 1172 (2013).

[22] https://uspex-team.org/en

[23] G. Kresse and J. Hafner, Phys. Rev. B **47**, 558 (1993).

[24] G. Kresse and J. Furthmüller, Comput. Mater. Sci. **6**, 15 (1996).

[25] G. Kresse and J. Furthmüller, Phys. Rev. B **54**, 11169 (1996).

[26] S. Arapan, P. Nieves, and S. Cuesta-López, J. Appl. Phys. **123**, 083904 (2018).

[27] P. E. Blöchl, Phys. Rev. B **50**, 17953 (1994).

[28] J. P. Perdew, K. Burke, and M. Ernzerhof, Phys. Rev. Lett. **77**, 3865 (1996).

[29] http://crono.ubu.es/novamag

[30] P. Nieves, S. Arapan, J. Maudes-Raedo, R. Marticorena-Sánchez, N. D. Brío, A. Kovacs, C. Echevarria-Bonet, D. Salazar, J. Weischenberg, H. Zhang *et al.*, Comput. Mater. Sci. **168**, 188 (2019).

[31] J. M. D. Coey, *Magnetism and Magnetic Materials* (Cambridge University Press, New York, 2010).

[32] V. Antropov, L. Ke, and D. Åberg, Solid State Commun. **194**, 35 (2014).

[33] X. Liu, D. Legut, R. Zhang, T. Wang, Y. Fan, and Q. Zhang, Phys. Rev. B **100**, 054438 (2019).

[34] A. Sommerfeld, Z. Phys. **47**, 1 (1928).

[35] D. Alfé, Comput. Phys. Commun. **180**, 2622 (2009).

[36] P. Vinet, J. R. Smith, J. Ferrante, and J. H. Rose, Phys. Rev. B **35**, 1945 (1987).

[37] A. Liechtenstein, M. Katsnelson, V. Antropov, and V. Gubanov, J. Magn. Magn. Mater. **67**, 65 (1987).

[38] M. I. Katsnelson and A. I. Lichtenstein, Phys. Rev. B **61**, 8906 (2000).

[39] H. Ebert, Rep. Prog. Phys. **59**, 1665 (1996).

[40] O. Eriksson, A. Bergman, L. Bergqvist, and J. Hellsvik, *Atomistic Spin Dynamics Foundations and Applications* (Oxford University Press, New York, 2017).

[41] B. Skubic, J. Hellsvik, L. Nordström, and O. Eriksson, J. Phys.: Condens. Matter **20**, 315203 (2008)

[42] http://www.physics.uu.se/research/materials-theory/ongoingresearch/uppasd

[43] R. Smallman and A. Ngan (eds.), *Modern Physical Metallurgy*, 8th ed. (Butterworth-Heinemann, Oxford, 2014), http://www.sciencedirect.com/science/article/pii/B9780080982045000171.

[44] H. Ding, S. S. Dwaraknath, L. Garten, P. Ndione, D. Ginley, and K. A. Persson, ACS Appl. Mater. Interfaces **8**, 13086 (2016).

[45] S. P. Ong, W. D. Richards, A. Jain, G. Hautier, M. Kocher, S. Cholia, D. Gunter, V. L. Chevrier, K. A. Persson, and G. Ceder, Comput. Mater. Sci. **68**, 314 (2013).

[46] W. Sun and G. Ceder, Surf. Sci. **617**, 53 (2013).

[47] S. Zhang and R. Zhang, Comput. Phys. Commun. **220**, 403 (2017).

[48] F. Mouhat and F. X. Coudert, Phys. Rev. B **90**, 224104 (2014).

[49] A. Zur and T. C. McGill, J. Appl. Phys. **55**, 378 (1984).

[50] P. Kumar, A. Kashyap, B. Balamurugan, J. E. Shield, D. J. Sellmyer, and R. Skomski, J. Phys.: Condens. Matter **26**, 064209 (2014).